# Baroclinic Instability in an Environment of Small Stability to Slantwise Moist Convection. Part I: Two-Dimensional Models

KERRY A. EMANUEL AND MAURIZIO FANTINI

*Center for Meteorology and Physical Oceanography, Massachusetts Institute of Technology, Cambridge, MA 02139*

ALAN J. THORPE

*Department of Meteorology, University of Reading, Reading, England*

(Manuscript received 6 October 1986, in final form 3 February 1987)

ABSTRACT

In the semigeostrophic system, the growth rate of baroclinic waves varies with the inverse square root of the potential vorticity, which acts as the effective static stability. Recent observations in the ascent regions of middle latitude cyclones show that the effective potential vorticity for saturated air is very near zero. In this paper we examine the structure and rate of growth of baroclinic cyclones when the effective potential vorticity is small for upward (saturated) displacements but large in regions of descent. Analytic solutions for two-dimensional disturbances in a two-layer semigeostrophic model and numerical simulations using a multilevel semigeostrophic model show that when the effective potential vorticity is small in regions of upward motion, growth rates are modestly increased and the region of ascent intensifies and collapses onto a thin ascending sheet. In the limit of zero moist potential vorticity the fastest growing wave has a finite growth rate which is about 2.5 times the dry value while the horizontal scale is reduced by a factor of about 0.6 compared to the dry modes. The asymmetry associated with condensation heating leads to frontal collapse first at the surface, rather than at both boundaries as in the dry case. In contrast to the analytic model, the numerical simulations allow the effect of (dry) potential vorticity evolution due to the latent heat release to be included. The anomalies of potential vorticity are advected horizontally through the wave, enhancing the low-level and diminishing the upper-level cyclonic vorticity and static stability in both the saturated and unsaturated regions of the flow.

## 1. Introduction

Recent observations within the ascent regions of middle latitude cyclones (e.g., Emanuel, 1985) reveal that the temperature lapse rate along absolute momentum ($M$) surfaces is very nearly moist adiabatic, having presumably been rendered such by slantwise moist convection. This condition has also been observed by the first author in cyclones surveyed during the Genesis of Atlantic Lows Experiment (GALE). Neutrality to slantwise convection has been shown by Bennetts and Hoskins (1979) to be equivalent to the condition of zero equivalent potential vorticity.

In the context of semigeostrophic theory (e.g., Hoskins and Bretherton, 1972) potential vorticity plays the same role as static stability does in quasi-geostrophy, with intrinsic length and time scales varying with the square root of the potential vorticity. As this quantity becomes small, as it effectively does in saturated regions within cyclones, the geostrophic momentum approximation becomes progressively weaker and breaks down altogether at zero potential vorticity, implying large ageostrophic accelerations (Emanuel, 1985). However, it is possible that despite a local breakdown in balanced motion the solutions described by these equations remain valid everywhere except in the immediate vicinity of the breakdown (Cullen and Purser, 1984). Here turbulence becomes important and, in effect, prevents the ultimate collapse of scale implied by the inviscid equations. With the above qualification we feel it is of importance and interest to explore the behavior of such systems with balance approximations near the limits of their validity. Future work with primitive equations will explore the accuracy of the balanced system.

In this spirit Emanuel (1985) and Thorpe and Emanuel (1985) explored the nature of frontal circulations and frontogenesis in environments which are nearly neutral to slantwise moist convection. The main effect of this condition is to cause the updraft to collapse down to very small scale and to somewhat enhance the rate of surface frontogenesis. Condensation increases the potential vorticity at low levels and diminishes it aloft, preserving the mass-weighted volume integral. These solutions are of particular interest as the latent heat release is strictly governed by the observed condition of near-zero moist potential vorticity.

In the present paper we wish to explore the somewhat broader issue of the effects of latent heat release on the development and structure of baroclinic waves, taking

near-zero moist potential vorticity as the relevant constraint on the rate of release of latent heat. In the following section we specifically relate the rate of heating to vertical velocity and moist and dry potential vorticity. We subsequently develop a set of semigeostrophic equations governing the development of $y$-independent disturbances on a zonal flow which varies only in the vertical. These are further specialized to a two-layer model in section 4 and analytic solutions are obtained. The full set of equations is solved numerically in section 5 using a multilevel semigeostrophic model and the solutions compared with the analytic results. Section 6 contains a discussion and concluding remarks.

## 2. Condensation heating

We derive the condensation heating in terms of moist and dry potential vorticity directly from the conservation of moist entropy (or equivalent potential temperature, $\theta_e$). Defining $s(=C_p \ln\theta)$ and $s^*(=C_p \ln\theta_e)$ as the dry and moist entropies, we write the conservation equation for $s^*$ as

$$\frac{ds^*}{dt}=\left(\frac{\partial s^*}{\partial t}+\mathbf{V}\cdot\nabla s^*\right)_p+\omega\frac{\partial s^*}{\partial p}=0, \tag{1}$$

where $\mathbf{V}$ is the vector horizontal velocity along constant pressure surfaces and the other symbols have their usual meanings. Now where air is saturated, $s^*$ is a state variable which we may consider to be a function of any other two state variables; in this case we choose $s$ and $p$. Therefore,

$$(ds^*)_p=\left(\frac{\partial s^*}{\partial s}\right)_p ds.$$

Using this, (1) may be written

$$\left(\frac{\partial s^*}{\partial s}\right)_p\left[\frac{\partial s}{\partial t}+\mathbf{V}\cdot\nabla s\right]+\omega\frac{\partial s^*}{\partial p}=0,$$

or

$$\frac{\partial s}{\partial t}+\mathbf{V}\cdot\nabla s=-\omega\left(\frac{\partial s}{\partial s^*}\right)_p\frac{\partial s^*}{\partial p}. \tag{2}$$

The total change of dry entropy, $s$, may thus be written

$$\frac{ds}{dt}=\frac{\partial s}{\partial t}+\mathbf{V}\cdot\nabla s+\omega\frac{\partial s}{\partial p}=\omega\left[\frac{\partial s}{\partial p}-\left(\frac{\partial s}{\partial s^*}\right)_p\frac{\partial s^*}{\partial p}\right]. \tag{3}$$

The quantity $(\partial s/\partial s^*)_p$ may be related to the moist and dry adiabatic lapse rates as follows. Regarding $s$ as a function of $p$ and specific volume, $\alpha$, we have

$$\left(\frac{\partial s}{\partial s^*}\right)_p=\left(\frac{\partial s}{\partial \alpha}\right)_p\left(\frac{\partial \alpha}{\partial s^*}\right). \tag{4}$$

From the first law of thermodynamics it can be shown that

$$\left(\frac{\partial s}{\partial \alpha}\right)_p=\frac{C_p}{\alpha}$$

$$\left(\frac{\partial \alpha}{\partial s^*}\right)_p=\left(\frac{\partial T}{\partial p}\right)_{s^*},$$

where $C_p$ is the heat capacity at constant pressure. The second relationship is derived in Emanuel (1986), appendix A. Using these, (4) becomes

$$\left(\frac{\partial s}{\partial s^*}\right)_p=\frac{C_p}{\alpha}\left(\frac{\partial T}{\partial p}\right)_{s^*}=\frac{\Gamma_m}{\Gamma_d}, \tag{5}$$

where $\Gamma_m=-(\partial T/\partial z)_{s^*}$ is the moist adiabatic lapse rate, $\Gamma_d$ is the dry adiabatic lapse rate, and we have made use of the hydrostatic approximation. Applying (5), (3) becomes

$$\frac{ds}{dt}=\omega\left[\frac{\partial s}{\partial p}-\frac{\Gamma_m}{\Gamma_d}\frac{\partial s^*}{\partial p}\right]. \tag{6}$$

We define geostrophic coordinates analogous to those used by Hoskins and Bretherton, (1972):

$$X=x+v_g/f,$$

$$Y=y-u_g/f,$$

$$P=p,$$

$$\tau=t, \tag{7}$$

where $f$ is the Coriolis parameter and $v_g$ and $u_g$ are the meridional and zonal components of the geostrophic wind. If we follow the same steps leading to (6), the heating formulation in geostrophic coordinates is

$$\frac{ds}{dt}=\omega\left[\frac{\partial s}{\partial P}-\frac{\Gamma_m}{\Gamma_d}\frac{\partial s^*}{\partial P}\right],$$

where it is understood that the pressure derivatives hold $X$, $Y$ and $\tau$ constant. From the definitions of $s$ and $s^*$, the above may alternatively be expressed

$$\frac{d\ln\theta}{dt}=\omega\left[\frac{\partial \ln\theta}{\partial P}-\frac{\Gamma_m}{\Gamma_d}\frac{\partial \ln\theta_e}{\partial P}\right]. \tag{8}$$

Through the remainder of this paper we shall work in height coordinates, making the approximation that $\omega \approx -\rho g w$. Then (8) becomes

$$\frac{d\ln\theta}{dt}=w\left[\frac{\partial \ln\theta}{\partial Z}-\frac{\Gamma_m}{\Gamma_d}\frac{\partial \ln\theta_e}{\partial Z}\right], \tag{9}$$

where $Z$ $(=z)$ is the geostrophic height coordinate. These diabatic terms are related to the potential vorticities based on $\theta$ and $\theta_e$. In geostrophic coordinates we can define

$$q_g=\frac{g\eta_g}{f}\frac{\partial}{\partial Z}\ln\theta=\frac{g\rho}{f\theta}\left(\frac{1}{\rho}\boldsymbol{\eta}\cdot\nabla\theta\right)$$

$$q_{ge}=\frac{g\eta_g}{f}\frac{\partial}{\partial Z}\ln\theta_e=\frac{g\rho}{f\theta_e}\left(\frac{1}{\rho}\boldsymbol{\eta}\cdot\nabla\theta_e\right) \tag{10}$$

where $\boldsymbol{\eta}\equiv\nabla\times v_g$, $\eta_g$ is the vertical component of $\boldsymbol{\eta}$, and the bracketed terms are the potential vorticity and equivalent potential vorticity, which are conserved in unsaturated and saturated flow, respectively (see Hoskins et al., 1985, for a review of potential vorticity concepts). In the following we shall take the density $\rho$ to be constant for simplicity, although this is not essential to the analysis. Consequently, $q_g$ and $q_{ge}$ are also conserved in Boussinesq flows. The relations (10) allow us to write (9) in the form[1]

$$\frac{d\ln\theta}{dt}=\frac{w^*}{g}\left[q_g-\frac{\Gamma_m}{\Gamma_d}q_{ge}\right], \tag{11}$$

where

$$w^*\equiv fw/\eta_g. \tag{12}$$

It is understood that (11) applies only in saturated flow, otherwise $\theta$ is conserved. We shall use (11) as the representation of condensation heating in the following development.

## 3. Semigeostrophic Eady model with condensation heating

We here develop the inviscid, Boussinesq semigeostrophic equations governing the development of $y$-independent perturbations on a base state zonal flow which is itself independent of $y$. The full semigeostrophic equations are (see Hoskins, 1975):

$$\left(\frac{\partial}{\partial\tau}+u_g\frac{\partial}{\partial X}+v_g\frac{\partial}{\partial Y}+w\frac{\partial}{\partial Z}\right)u_g-fv_a=0, \tag{13}$$

$$\left(\frac{\partial}{\partial\tau}+u_g\frac{\partial}{\partial X}+v_g\frac{\partial}{\partial Y}+w\frac{\partial}{\partial Z}\right)u_g+fu_a=0, \tag{14}$$

$$\left(\frac{\partial}{\partial\tau}+u_g\frac{\partial}{\partial X}+v_g\frac{\partial}{\partial Y}+w\frac{\partial}{\partial Z}\right)\ln\theta=\frac{d\ln\theta}{dt}, \tag{15}$$

where the independent coordinates are defined by (7) but with $Z=z$. The horizontal ageostrophic wind components are $u_a$ and $v_a$. The system is closed using the thermal wind relations and the mass continuity equation, the last of which we write in physical coordinates:

$$f\frac{\partial u_g}{\partial Z}=-g\frac{\partial\ln\theta}{\partial Y}, \tag{16}$$

$$f\frac{\partial v_g}{\partial Z}=g\frac{\partial\ln\theta}{\partial X}, \tag{17}$$

$$\frac{\partial u}{\partial x}+\frac{\partial v}{\partial y}+\frac{\partial w}{\partial z}=0. \tag{18}$$

A time-independent zonal flow of the form $u_g=u_g(z)$ and an associated meridional gradient of $\ln\theta$ obeying (16) are solutions of this system of equations. As a particular case, we take $u_g=u_{gz}(Z-H/2)$, where $u_{gz}$ is a constant and $H$ is the vertical distance between two parallel plates. The associated meridional gradient of $\ln\theta$, from (16), is then constant. If (15) is differentiated in $Y$, the result is

$$\left(\frac{\partial}{\partial\tau}+u_g\frac{\partial}{\partial X}+v_g\frac{\partial}{\partial Y}+w\frac{\partial}{\partial Z}\right)\frac{\partial\ln\theta}{\partial Y}$$
$$=\frac{\partial}{\partial Y}\frac{d\ln\theta}{dt}-\frac{\partial u_g}{\partial Y}\frac{\partial\ln\theta}{\partial X}-\frac{\partial v_g}{\partial Y}\frac{\partial\ln\theta}{\partial Y}-\frac{\partial w}{\partial Y}\frac{\partial\ln\theta}{\partial Z}.$$

This shows that if the heating and velocity perturbations are independent of $Y$, $\partial\ln\theta/\partial Y$ is constant for all time. This in turn implies that $u_g$ is time-independent. Without loss of generality, then, we write

$$u_g=u_{gz}(Z-H/2),$$

$$\ln\theta=-\frac{f}{g}u_{gz}Y+\ln\theta(X,Z,\tau).$$

With these substitutions, (13)–(15) become

$$wu_{gz}=fv_a, \tag{19}$$

$$\left(\frac{\partial}{\partial\tau}+u_g\frac{\partial}{\partial X}+w\frac{\partial}{\partial Z}\right)v_g=-fu_a, \tag{20}$$

$$\left(\frac{\partial}{\partial\tau}+u_g\frac{\partial}{\partial X}+w\frac{\partial}{\partial Z}\right)\ln\theta=\frac{d\ln\theta}{dt}+\frac{f}{g}u_{gz}v_g. \tag{21}$$

Finally, the mass continuity equation (18) together with the coordinate transformations (7) may be used to define a streamfunction $\psi$ such that

$$u_a=-\frac{\partial\psi}{\partial z}=-\frac{\partial\psi}{\partial X}\frac{\partial\psi}{\partial z}-\frac{\partial\psi}{\partial Z}\frac{\partial Z}{\partial z}=-\frac{1}{f}\frac{\partial v_g}{\partial z}\frac{\partial\psi}{\partial X}-\frac{\partial\psi}{\partial Z}$$
$$=\frac{-\eta_g}{f^2}\frac{\partial v_g}{\partial Z}\frac{\partial\psi}{\partial X}-\frac{\partial\psi}{\partial Z},$$

$$w=\frac{\partial\psi}{\partial x}=\frac{\partial\psi}{\partial X}\frac{\partial X}{\partial x}=\frac{\eta_g}{f}\frac{\partial\psi}{\partial X}. \tag{22}$$

With these relations, (19)–(21) and (17) can be written, using the heating formulation (11),

$$fv_a=\frac{\eta_g}{f}u_{gz}\frac{\partial\psi}{\partial X}, \tag{23}$$

$$\left(\frac{\partial}{\partial\tau}+u_g\frac{\partial}{\partial X}\right)v_g=f\frac{\partial\psi}{\partial Z}, \tag{24}$$

[1] Thorpe and Emanuel (1985) omitted the coefficient $\Gamma_m/\Gamma_d$ which appears in (11) due to an oversight. As they were principally concerned with flows in the limits of small $q_{ge}$, however, the omisison leads to only very small quantitative errors.

$$g\left(\frac{\partial}{\partial\tau}+u_g\frac{\partial}{\partial X}\right)\ln\theta+q\frac{\partial\psi}{\partial X}=fu_{gz}v_g, \tag{25}$$

$$f\frac{\partial v_g}{\partial Z}=g\frac{\partial\ln\theta}{\partial X}, \tag{26}$$

where $q$ is defined separately in saturated and unsaturated regions:

$$q\equiv\begin{cases}q_g, & \text{unsaturated}\\ \dfrac{\Gamma_m}{\Gamma_d}q_{ge}, & \text{saturated.}\end{cases} \tag{27}$$

It remains only to determine the evolution equations for $q_g$ and $q_{ge}$. The latter is exactly conserved in flow which is either saturated or two-dimensional (Bennetts and Hoskins, 1979):

$$\frac{dq_{ge}}{dt}=0. \tag{28}$$

The basic equation for $q_g$ may be written (e.g., Thorpe and Emanuel, 1985):

$$\frac{dq_g}{dt}=g\frac{\eta_g}{f}\frac{\partial}{\partial Z}\frac{d\ln\theta}{dt}.$$

Using (11) and (22) this becomes, in saturated regions only,

$$\frac{dq_g}{dt}=\frac{\eta_g}{f}\frac{\partial}{\partial Z}\left[\frac{\partial\psi}{\partial X}\left(q_g-\frac{\Gamma_m}{\Gamma_d}q_{ge}\right)\right]. \tag{29}$$

Otherwise, $q_g$ is conserved.

The system comprised of (24)–(29) is a closed set of equations for $\psi$, $v_g$, $\ln\theta$, $q_g$, and $q_{ge}$, while (23) may be used to diagnose $v_a$. Although $\Gamma_m$ is strictly a function of pressure and temperature, its variability is mostly with height in a domain whose horizontal size scales with the deformation radius. For simplicity, we regard $\Gamma_m$ as a fixed function of $Z$. We also note that a prediction equation for water substance is necessary to determine whether the air is saturated. As our aim is to describe the essential physics of baroclinic waves with condensation, however, we shall simply assume that ascending air is saturated while descending air remains dry. In terms of observations, this is seldom far from the truth.

## 4. A two-layer model

We shall now derive analytic solutions to the systems of equations described in section 3 for the crudest nontrivial vertical discretization of the system, which can be described as a two-layer model (Phillips, 1951). The structure of such a model is illustrated in Fig. 1. We require that the streamfunction vanish along the upper and lower boundaries, and define meridional geostrophic velocities $v_1$ and $v_2$ at the midpoints of each layer. Streamfunction and potential temperature are defined at the interface between the two layers. The

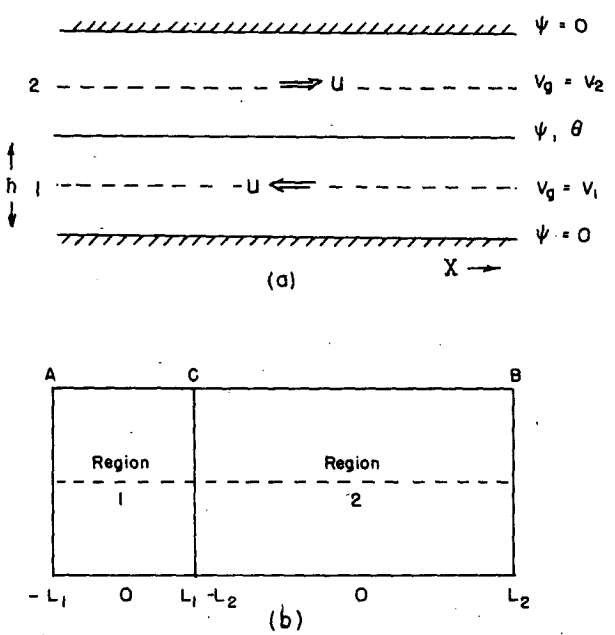


FIG. 1. Structure of the two-layer model. The subdivision of layers and levels where quantities are defined is shown in (a), while the division into moist and dry regions is illustrated in (b). The $X$ coordinate is defined separately in each region, extending from $-L_1$ to $L_1$ in region 1 and from $-L_2$ to $L_2$ in region 2. The perturbations are periodic so that quantities are matched at points A and B and at point C.

model domain is taken in a reference frame moving at the vertical mean speed of the zonal geostrophic wind so that the zonal velocities at the midpoints of each layer are

$$u_1\equiv -U=-u_{gz}h/2,$$

$$u_2\equiv U=u_{gz}h/2,$$

where $h$ is half the depth of the domain. With these definitions, the vertical discretization of (24)–(26) gives

$$\left(\frac{\partial}{\partial\tau}+U\frac{\partial}{\partial x}\right)v_2=-f\psi/h, \tag{30}$$

$$\left(\frac{\partial}{\partial\tau}-U\frac{\partial}{\partial x}\right)v_1=f\psi/h, \tag{31}$$

$$g\frac{\partial}{\partial\tau}\ln\theta+q\frac{\partial\psi}{\partial X}=\frac{1}{2}fu_{gz}(v_1+v_2), \tag{32}$$

$$f(v_2-v_1)=gh\frac{\partial\ln\theta}{\partial X}, \tag{33}$$

with $q$ defined by (27). Except for the middle term in (32), this is a linear system. The (partial) linearization of this term uses the initial value of $q_g$ rather than a time-dependent value derived from (29). Thus we approximate (27) by

$$q \equiv \begin{cases} q_{g0} & w \leq 0 \\ \dfrac{\Gamma_m}{\Gamma_d} q_{ge} & w > 0, \end{cases} \tag{34}$$

where $q_{g0}$ is the initial value of $q_g$, assumed constant. If we take $q_{ge}$ to be initially constant, it will remain constant by (28) for either two-dimensional or saturated motion. Thus it is important to note that *the neglect of the temporal variability of $q_g$ is the only linearization we will make.*

The number of parameters in (30)–(34) may be reduced through a suitable choice of normalizations. Denoting dimensional variables by tildes, these are

$$\begin{aligned} \tilde{X} &= h q_{g0}^{1/2} f^{-1} X, \\ \tilde{\tau} &= f^{-1} h q_{g0}^{1/2} U^{-1} \tau, \\ (\tilde{v}_1, \tilde{v}_2) &= h q_{g0}^{1/2} (v_1, v_2), \\ \tilde{\psi} &= h U \psi, \\ \widetilde{\ln\theta} &= q_{g0} h g^{-1} \theta, \\ \tilde{q} &= q_{g0} q. \end{aligned} \tag{35}$$

Note that $2hq_{g0}^{1/2}/f$ is the analog of the Rossby radius of deformation in the semigeostrophic model, and that $h$ is the *half*-depth of the layer. If we seek exponentially growing solutions of the form $\exp(\sigma\tau)$, (where $\sigma$ may be complex), then (30)–(34) become, with the normalizations (35)

$$\left(\sigma + \frac{\partial}{\partial X}\right) v_2 = -\psi, \tag{36}$$

$$\left(\sigma - \frac{\partial}{\partial X}\right) v_1 = \psi, \tag{37}$$

$$\sigma\theta + q\frac{\partial \psi}{\partial X} = v_1 + v_2, \tag{38}$$

$$v_2 - v_1 = \frac{\partial \theta}{\partial X}, \tag{39}$$

$$q \equiv \begin{cases} 1, & \dfrac{\partial \psi}{\partial X} \leq 0 \\ r, & \dfrac{\partial \psi}{\partial X} > 0, \end{cases} \tag{40}$$

where

$$r \equiv \frac{\Gamma_m}{\Gamma_d} \frac{q_{ge}}{q_{g0}}. \tag{41}$$

It is assumed that $r$ is a constant. The dependent variables in (36)–(39) may be eliminated in favor of $\psi$ to yield the fourth-order equation

$$2\left(\sigma^2 + \frac{\partial^2}{\partial X^2}\right)\psi - \left(\sigma^2 - \frac{\partial^2}{\partial X^2}\right)\frac{\partial}{\partial X}\left(q\frac{\partial \psi}{\partial X}\right) = 0. \tag{42}$$

In the dry case [$r = 1$ in (40)], the preceding has a simple solution of the form $\psi = \psi_0 \exp[ikX]$, where $k$ is a horizontal wavenumber. The solution for $\sigma^2$ is then

$$\sigma^2 = k^2 \frac{2 - k^2}{2 + k^2},$$

for which the maximum value of $\sigma$ is $2 - \sqrt{2}$ (=0.586) occuring at a $k^2$ of $2(\sqrt{2} - 1)$. This is the classical result of the two-layer model, though the dimensional equivalent quantities involve the potential vorticity rather than the static stability. (The continuous Eady model has a maximum value of $\sigma$ of 0.62 occurring at a $k^2$ of 0.65.)

When $r \neq 1$ in (40), the problem becomes nonlinear due to the dependence of $r$ on the sign of $w$. The equations are, however, linear except at points where $w$ changes sign. It is then possible to solve (42) in piecewise segments where $w$ has a single sign and match the solutions across points where $w$ changes sign. In order to carry this procedure out, we assume that $\psi$ is periodic over a length $2L$ and that $w$ changes sign only twice in this interval (see Fig. 1b). The vertical velocity is taken to be negative in region 2 and positive in region 1. Though we shall be able to find solutions of this character, there is no a priori reason to suppose they are unique.

According to (40), $q$ is constant in the interiors of regions 1 and 2, so that (42) may be written

$$q\frac{\partial^4 \psi}{\partial X^4} + (2 - \sigma^2 q)\frac{\partial^2 \psi}{\partial X^2} + 2\sigma^2 \psi = 0. \tag{43}$$

This is solved in each region and the solutions matched at points C and A (=B) in Fig. 1b. We require that $\partial\psi/\partial X$ be positive in region 1 and negative in region 2.

The matching conditions are derived by demanding continuity of $\psi$ and pressure at the levels where they are defined. Using (36)–(39) it can be shown that the four conditions may be phrased as the continuity of the following functions of $\psi$:

$$\psi,\ q\frac{\partial \psi}{\partial X},\ \frac{\partial}{\partial X}\left(q\frac{\partial \psi}{\partial X}\right),$$

$$2\frac{\partial \psi}{\partial X} + \frac{\partial^2}{\partial X^2}\left(q\frac{\partial \psi}{\partial X}\right).$$

The interior equations (43) have only even derivatives and the aforementioned matching conditions are in terms of either odd or even derivatives, but not both kinds together. If we define a separate $X$ coordinate in each of the two regions of Fig. 1b, the solutions in each region may be separated into symmetric and antisymmetric parts, $\psi_s$ and $\psi_a$, such that

$$\begin{aligned} 2\psi_s(X) &= \psi(X) + \psi(-X), \\ 2\psi_a(X) &= \psi(X) - \psi(-X), \end{aligned}$$

in each region. The matching conditions and thus the eigenvalues will be different for $\psi_a$ and $\psi_s$. But since

we demand that $w = \partial\psi/\partial X$ not change sign within a region, we must discard the symmetric solutions in favor of $\psi_a$. This symmetry will facilitate the search for solutions.

Finally, we note in (44) that $q\partial\psi/\partial X$ must be continuous across points C and A (=B), where $w$ itself is assumed to change sign. Since $q$ does not change sign, $q\partial\psi/\partial X$ must do so and since it is continuous it must vanish at these points. Thus we enforce the condition that $\partial\psi/\partial X$ vanish at A, B and C. This is an additional constraint that further limits the eigenvalues and in fact makes it impossible to find solutions for arbitrary widths of the regions 1 and 2. Thus the relative widths of the up- and downdrafts are themselves eigenvalues.

The method of solution of the eigenvalue problem is described in appendix A; it suffices to say here that we treat the system as a double eigenvalue problem for the eigenvalues $\sigma$ and $\lambda$, where the latter is the ratio of the updraft to the downdraft width, having fixed the values of $r$ and $L$. In appendix B we prove that $\sigma$ is never complex.

The eigenvalues $\sigma$ are shown in Fig. 2 as a function of the downdraft half-width $L_2$ for different values of $r$. The *total* wavelength $[=2L_2(1+\lambda)]$ at which $\sigma$ peaks decreases with $r$, as does the ratio of the updraft to the downdraft width. The shortwave cutoff in terms of $L_2$ remains constant with the value $\pi/(2\sqrt{2})$ but decreases in terms of $L$ by nearly a factor of 2 at $r = 0$. The growth rate $\sigma$ increases with decreasing $r$. The growth rate maximized with respect to $L$ is shown in Fig. 3 as a function of $r$ together with $L$, $\lambda$, and the downdraft width. The last of these quantities increases slowly with diminishing $r$, while the total wavelength and updraft width diminish.

The maximum growth rate shown in Fig. 3 evidently does not become indefinitely large as $r$ approaches zero, as it would if the potential vorticity become small everywhere, not just in the updraft. The asymptotic analysis presented in appendix C shows that the growth rate approaches the limiting value 1.484 as $r \to 0$. According to the nondimensionalizations (35) the minimum dimensional $e$-folding time is then

$$\tau_e = \frac{h}{U}\frac{\sqrt{q_{g0}}}{1.484f} = \frac{1.348}{u_{gz}}\frac{\sqrt{q_{g0}}}{f}.$$

This is a factor of 0.395 of the $e$-folding time in the dry case. For a vertical shear of 5 m s$^{-1}$/km, $q_{g0} = 10^{-4}$ s$^{-2}$ and $f = 10^{-4}$ s$^{-1}$ this amounts to about 7.5 hours. This is a major result of this work and gives the first indication that the presence of moist processes in baroclinic waves does not lead to an "ultraviolet" catastro-

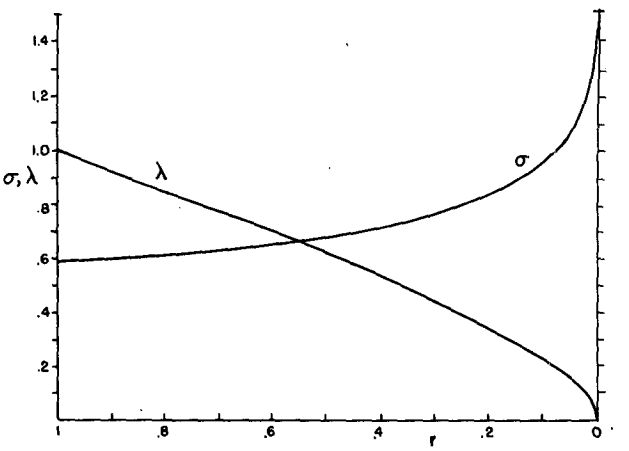


FIG. 3a. The maximum growth rate $\sigma$ and ratio $\lambda$ of updraft to downdraft widths as a function of $r$.

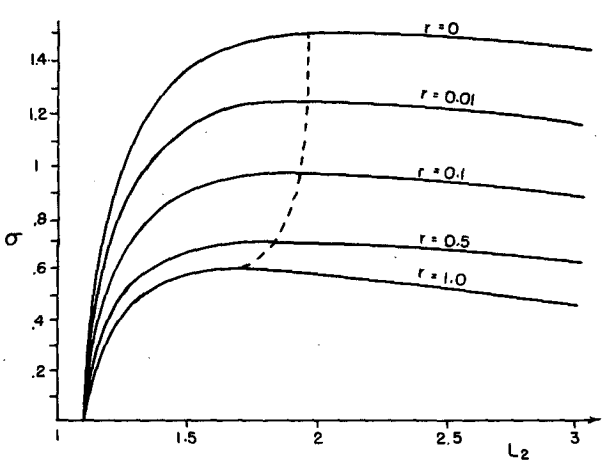


FIG. 2. The growth rate $\sigma$ as a function of the half-width of the dry region, $L_2$, for different values of $r$. The curve for $r = 0$ is derived in appendix C. The dashed line connects the growth rate maxima of each curve.

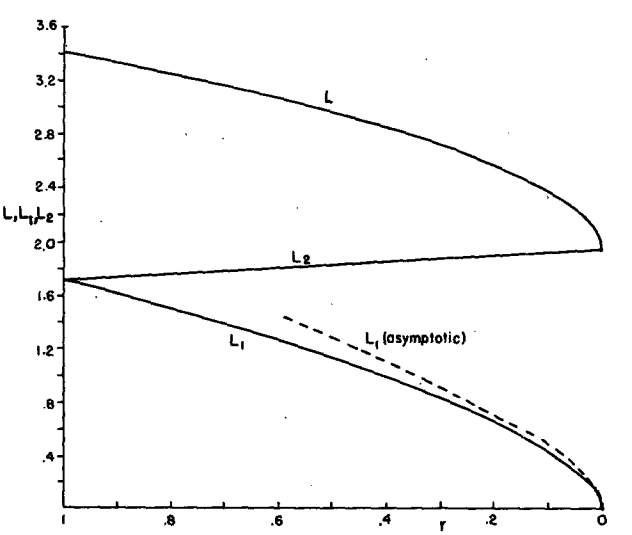


FIG. 3b. The updraft half-width $L_1$, downdraft half-width $L_2$, and total half-wavelength $L = (L_1 + L_2)$ corresponding to the maximum growth rate, as a function of $r$. The dashed line shows the asymptotic solution for $L_1$ derived in appendix C.

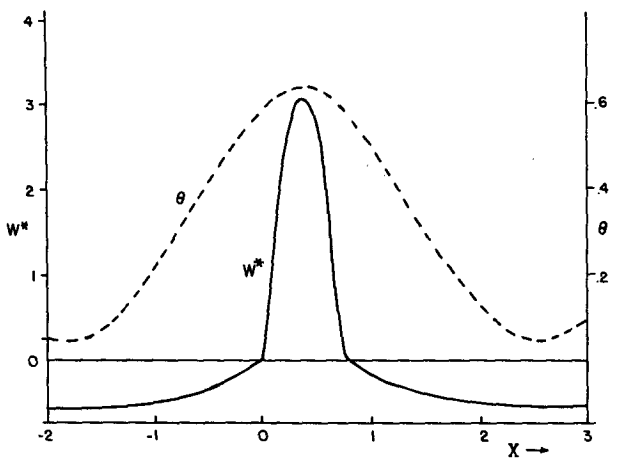


FIG. 4a. The modified dimensionless vertical velocity, $w^*$, and dimensionless potential temperature $\theta$, each defined at the model mid-level, as a function of the geostrophic coordinate $X$ for the most rapidly growing solutions when $r = 0.08$.

phe in which the shortest scales grow indefinitely rapidly. We can hence give a limit to the growth rate of a normal-mode moist baroclinic development in the absence of surface fluxes of heat and moisture.

In the limiting case of small $r$ the updraft width becomes vanishingly small. In appendix C it is shown that in the limit of small $r$, the updraft half-width $L_1 \to \pi\sqrt{r}/(2\sqrt{2}) + r$. As suggested by Fig. 2, the growth rate peak with respect to the total wavelength becomes progressively less well defined, but still has a peak at $r = 0$. This peak shows that the most rapidly growing moist mode with zero stability to slantwise moist convection has a total horizontal wavelength of about 0.6 times that for the maximum growing dry mode. Using the values above and a half-depth $h$ of 5 km gives a dimensional wavelength of about 1940 km for the moist wave. As shown in appendix C, the growth rate when $r = 0$ asymptotes to $\sqrt{2}$ at large $L$. Thus, paradoxically, the longwaves are destabilized by condensation even though the most rapidly growing disturbance shifts to smaller scale. The scale selectivity at scales longer than that associated with the fastest growing mode is very weak when $r$ is near zero.

The horizontal structures of the various fields are shown in Fig. 4 for the case $r = 0.08$ with $L$ near the wavelength of maximum growth. The most obvious effect of condensation is to narrow and intensify the updraft and weaken and broaden the downdraft. The pressure and temperature fields are still remarkably sinusoidal (in geostrophic coordinates), though the low-level pressure trough and upper ridge are slightly enhanced compared to their counterparts. The temperature perturbation is everywhere positive, showing the effect of net latent heat release. In the Boussinesq approximation, only the gradients of $\ln\theta$ appear, so that this net heating does not affect the dynamics. Associated with this effect is a domain-average pressure fall at the lower level and pressure increase at the upper level.

To obtain some idea of the wave structure in physical space we extrapolate the linear result to finite amplitude. In doing so, the only nonlinearity we neglect is that associated with the change in dry potential vorticity given by (29) which, due to the near symmetry, will be generally small at the midlevel, where potential vorticity enters the two-level model equations. Specifically, we select an amplitude such that the maximum absolute vorticity at level 1 is $10f$; i.e., at a time when a discontinuity is about to form at low levels. The resulting fields in physical space are shown in Fig. 5. Notable features of these fields include:

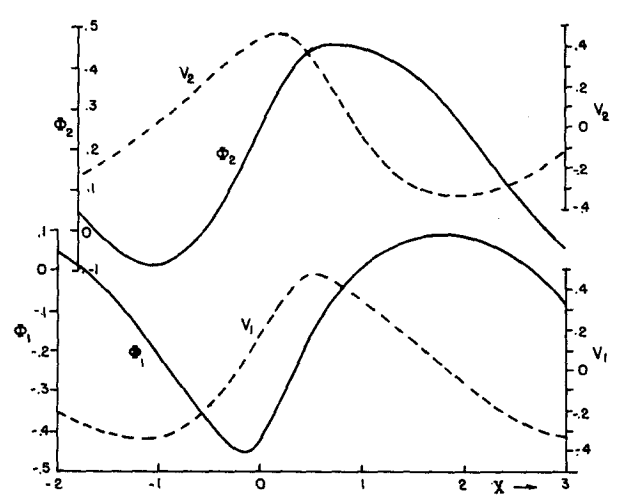


FIG. 4b. As in (a) except for dimensionless meridional velocities, $v$, and modified pressures, $\Phi$, defined in the upper and lower layers. ($\Phi = \frac{p}{\rho} + \frac{1}{2}v^2$.)

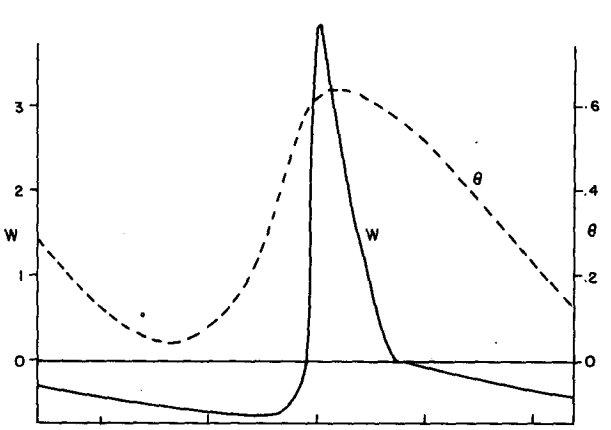


FIG. 5a. As in Fig. 4a except showing real dimensionless vertical velocity, $w$, and $\theta$ in physical coordinates for an amplitude at which the maximum low-level vorticity is 10f.

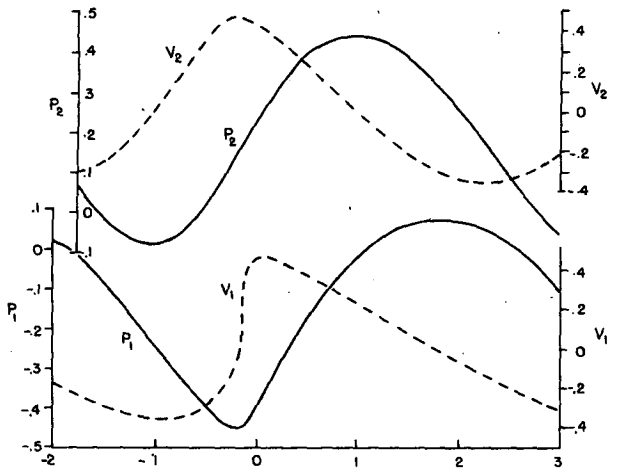


FIG. 5b. As in (a) except for dimensionless meridional velocities, $v$, and real pressures, $p$, in the upper and lower layers.

1) Frontal collapse occurs at low levels first. (In the dry model, singularities appear at the lower and upper level simultaneously.) This is clearly related to the large stretching effect on vorticity associated with the strong updraft.

2) The western edge of the updraft is extremely sharp while the eastern side is more gradual. The strongest descent is just to the rear of the surface pressure trough.

3) While the surface pressure pattern is strongly asymmetric, showing a broad ridge and sharp trough, the upper-level pressure wave is nearly sinusoidal. The associated meridional wind field is strongly asymmetric at the lower level but only modestly so aloft.

Although this model cannot resolve the vertical structure of the vertical velocity, the numerical simulations described in section 5 show that the updraft tends to be aligned along constant $X$ surfaces. These surfaces slope westward with height when the vertical shear of the meridional wind is positive with the converse holding as well. Careful inspection of Fig. 5 shows that $X$ surfaces slope westward with height on the western side of the updraft and eastward with height near the east edge of the region of upward motion, implying the characteristic wedge shape of the updraft first noted by Bjerknes (1919). In order to further resolve the vertical structure of the disturbances and account for the effects of changing potential vorticity, we turn in the following section to numerical integration of the semigeostrophic equations.

## 5. Numerical simulations

The numerical solution of the equation set involves using Eq. (29) to determine the time development of the potential vorticity $q_g$. The geostrophically balanced flow consistent with the current distribution of $q_g$ is determined by the inversion equation, which is obtained from the definition of $\eta_g$ using geostrophic and hydrostatic balance:

$$\frac{1}{f^2}\frac{\partial^2\Phi}{\partial X^2}+\frac{1}{q_g}\frac{\partial^2\Phi}{\partial Z^2}=1, \tag{44}$$

where $\Phi$ [$=\phi+\frac{1}{2}(u_g^2+v_g^2)$] is the modified geopotential and $\phi$ is the normal geopotential. This computation has been referred to as the invertibility principle by Hoskins et al. (1985). To solve Eq. (44) we need $q_g(X, Z)$ and the potential temperature on the two horizontal boundaries of the domain to specify $\partial\Phi/\partial Z$ as boundary conditions. Equation (25) is integrated numerically to give the time evolution of the boundary potential temperature:

$$g\left(\frac{\partial}{\partial\tau}+u_g\frac{\partial}{\partial X}\right)\ln\theta=u_{gz}\frac{\partial\Phi}{\partial X}\quad\text{on}\quad Z=0,2h. \tag{45}$$

Finally, to determine the ageostrophic streamfunction $\psi$ necessary to provide the source term in the potential vorticity equation, the Sawyer–Eliassen circulation equation is solved diagnostically each timestep. By taking $f[\partial(24)/\partial Z]-[\partial(25)/\partial X]$ and using the thermal wind relation we obtain:

$$f^2\frac{\partial^2\psi}{\partial Z^2}+\frac{\partial}{\partial X}\left(q\frac{\partial\psi}{\partial X}\right)=-2fu_{gz}\frac{\partial v_g}{\partial X}. \tag{46}$$

This equation is solved taking $w=0$ on the horizontal boundaries and periodic conditions on the lateral boundaries. The numerical algorithm uses the prognostic Eqs. (29) and (45) and the diagnostic Eqs. (44) and (46).

The equations are solved in a periodic domain with a variable horizontal dimension and in a layer of depth $2h=10$ km. The number of horizontal gridpoints is 128 while the vertical resolution is 250 m. Due to the coordinate transformation, a fixed horizontal gridlength corresponds to an increased resolution in physical space in regions of cyclonic vorticity. The finite difference scheme is centered in space and time with a 15-min timestep, which is reduced if the flow intensification requires this for stability. The elliptic equations are solved using periodic Fourier transforms in the $X$-direction and Gaussian elimination in the vertical (see Heckley, 1980, for details). The numerical simulations begin with $r=0.1$, using an initial potential vorticity of 0.327 PV units corresponding to values of $q_{g0}=1.36\times10^{-4}$ s$^{-2}$ and $2hq_{g0}^{1/2}/f=1167$ km. The shear $u_{gz}$ was taken as $3\times10^{-3}$ s$^{-1}$ or $U=15$ m s$^{-1}$ and $f=10^{-4}$ s$^{-1}$, $\rho=1.22$ kg m$^{-3}$, and $\theta_0=288$ K.

In the dry case, $r=1$, the normal model growth rate and structure has been described by Hoskins (1976) for this semigeostrophic model. For example, the dispersion relation is given by the expression:

$$\sigma^2=4(k\coth k-1)(1-k\tanh k).$$

The shortwave cutoff occurs at $k=1.2$ and the max-

imum growing mode has $\sigma = 0.62$ and $k = 0.80$. Note that these are slightly different from the values predicted by the two-layer model described earlier. The numerical simulations are all initiated with a small-amplitude dry normal mode with a surface $\theta$ perturbation of $\pm 2$ K. We shall describe four simulations, with figures shown for three of these. The following are essential characteristics of these simulations:

(i) $k = 0.80$, $2L = 4554$ km, dry (Fig. 6) and moist (Fig. 7). This wavelength corresponds to the fastest growing dry mode.

(ii) $k = 0.94$, $2L = 3900$ km, moist (Fig. 8). This moist wave grows the most rapidly of those to be described here.

(iii) $k = 1.27$, $2L = 2875$ km, moist. This corresponds to a neutral dry mode which, however, grows in the presence of moisture.

It should be noted that in these simulations the total half-wavelength $L$ cannot change during a particular integration, as it is fixed at the domain size, but the updraft and downdraft region $L_1$ and $L_2$ can evolve. As we begin with a dry normal mode at $t = 0$, then $L_1 = L_2 = L/2$. Consequently, for example, $L_1$ will decrease as the wave intensifies reaching a finite limit in transformed space. However, in physical space there is a continuing contraction as the fronts progress to discontinuities.

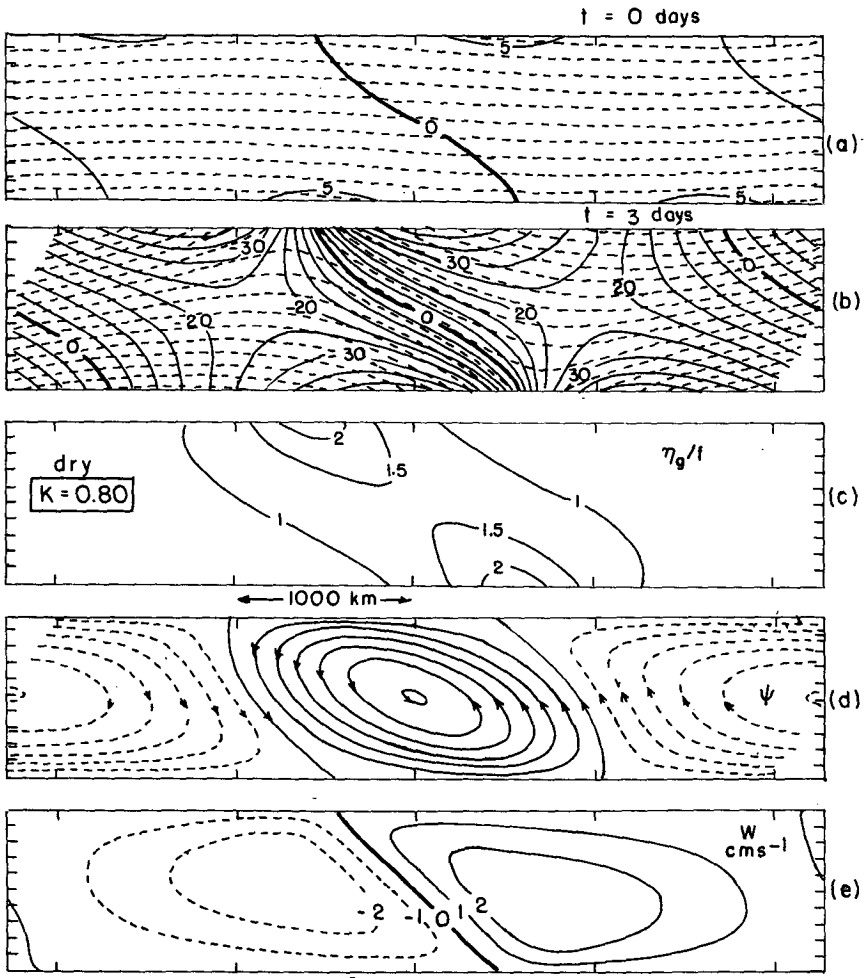


FIG. 6. The structure of the dry wave with $k = 0.80$ or wavelength 4554 km. Shown are horizontal–vertical contour plots with the horizontal axis marked with ticks every 1000 km and the vertical axis with ticks every 1 km. (a) The meridional flow (solid lines, contour interval 5 m $s^{-1}$) and the potential temperature $\theta$ (dashed lines, contour interval 4 K) at $t = 0$. This corresponds to a dry normal mode of small amplitude. (b) Meridional flow and $\theta$ at $t = 3$ days. (c) $\eta_g/f$ with contour interval of 0.5, at $t = 3$ days. (d) Streamfunction for the ageostrophic flow, contour interval of 4000 $m^2$ $s^{-1}$, at $t = 3$ days. (e) Vertical velocity with contour interval 1 cm $s^{-1}$, at $t = 3$ days.

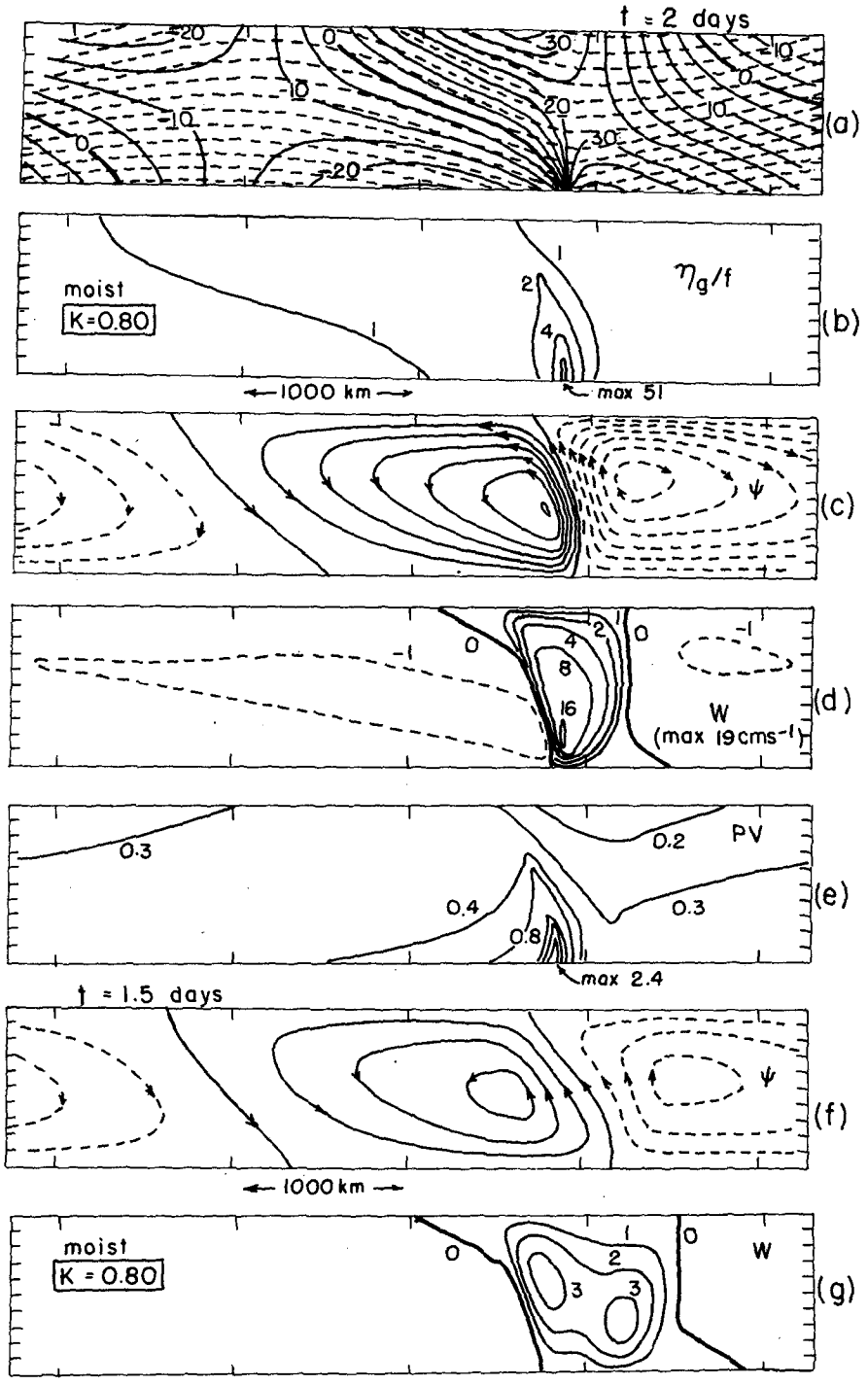


FIG. 7. The structure of the moist wave with $r = 0.1$ initially and $k = 0.80$ or wavelength 4554 km. Figures have the same format as Fig. 6 unless otherwise stated. (a) The meridional flow and $\theta$ at $t = 2$ days. (b) $\eta_g/f$ at $t = 2$ days. Note uneven contour interval. (c) Streamfunction at $t = 2$ days. Contour interval is 4000 $m^2 s^{-1}$. (d) Vertical velocity at $t = 2$ days. Note uneven contour interval. (e) Potential vorticity PV = $(1/\rho)\eta \cdot \nabla\theta$ at $t = 2$ days. The contours are labeled in PV units, where 1 PV unit = $10^{-6}$ K $m^{-2}$ $kg^{-1}$ $s^{-1}$. Note the uneven contour interval. The initial value was 0.327 PV units; to obtain $q_g$ a PV unit must be multiplied by $4.15 \times 10^{-4}$. (f) Streamfunction at $t = 1.5$ days. (g) Vertical velocity at $t = 1.5$ days. Contour interval 1 cm $s^{-1}$.

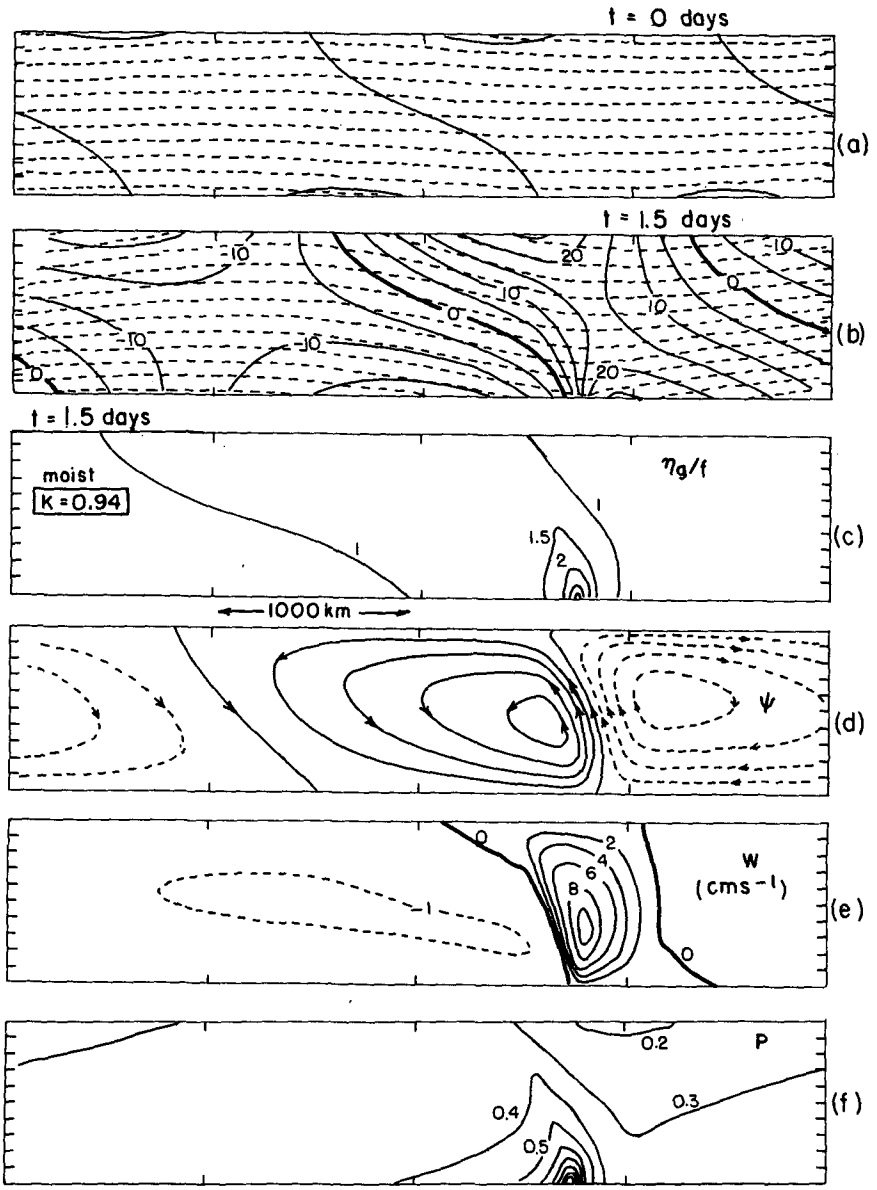


FIG. 8. The structure of the moist wave with $r = 0.1$ and $k = 0.94$ or wavelength 3900 km. Figures have the same format as Fig. 6 unless otherwise stated. (a) Meridional flow and $\theta$ at $t = 0$. (b) Meridional flow and $\theta$ at $t = 1.5$ days. (c) $\eta_g/f$ at $t = 1.5$ days. Contour interval 0.5. (d) Streamfunction at $t = 1.5$ days. Contour interval is 4000 m$^2$ s$^{-1}$. (e) Vertical velocity at $t = 1.5$ days. Contour interval 1 cm s$^{-1}$. (f) Potential vorticity [$=(1/\rho)\eta \cdot \nabla\theta$) at $t = 1.5$ days. The contour interval is 0.1 PV units, where a PV unit is $10^{-6}$ K m$^{-2}$ kg$^{-1}$ s$^{-1}$. The initial value was 0.327 PV units and to obtain $q_g$ a PV unit must be multiplied by $4.15 \times 10^{-4}$.

Figures 6, 7 and 8 all refer to physical space and show vertical ($z$)–horizontal ($x$) cross sections of the relevant fields. The geostrophic flow $v_g$ is shown superimposed with the isentropic distribution. Other fields include the normalized absolute vorticity, $\eta_g/f$, the streamfunction $\psi$, the vertical velocity $w$, and the (dry) potential vorticity.

We shall discuss the important features of these simulations under the following headings:

### *a. Horizontal scale*

From the vertical velocity fields we can see that while the dry mode (Fig. 6) retains $L_1 = L_2$, there is a considerable contraction in the horizontal scale of the region of ascent in the moist development. For example, in Fig. 8, at this stage in the wave growth, we estimate $\lambda = 0.15$. Note that this figure is in physical space rather than in transformed space as given in Fig. 3a. In trans-

formed space the value is closer to the value of 0.24 predicted in Fig. 3a.

*b. Growth rate*

This is a difficult quantity to obtain from the simulations for comparison with the two-layer model, as the initial (dry) mode is not a moist normal mode. Consequently there is a period of adjustment at the beginning of the integration as the moist mode becomes established; this is most apparent in Fig. 7 at $t = 1.5$ days, as will be discussed later. The following compares the time taken for the front to collapse to a discontinuity:

$$k = 0.80, \begin{cases} \text{dry:} & t \approx 3.7 \text{ days} \\ \text{moist:} & t = 2.01 \text{ days} \end{cases}$$

$$k = 0.94, \begin{cases} \text{dry:} & t \approx 3.7 \text{ days} \\ \text{moist:} & t = 1.71 \text{ days} \end{cases}$$

$$k = 1.27, \begin{cases} \text{dry:} & \text{no growth or discontinuity} \\ \text{moist:} & t = 2.2 \text{ days.} \end{cases}$$

Using these data and the rate of increase in amplitude of several variables it is possible to estimate that the moist mode grows between two and three times as fast as the dry waves. Considering that $r$ is initially 0.1, this suggests that the two-layer model may underestimate the increase in growth rate due to moist processes.

*c. Meridional geostrophic flow*

In the dry simulation the warm air maximum and the cold air minimum of meridional (or along-front) flow are equal in magnitude and symmetrical in the lower and upper parts of the domain. There is a small asymmetry in the vertical in the moist case but the main asymmetry is that the warm southerly flow is substantially stronger than the cold northerly flow. This feature is also apparent in the two-layer solutions, though to a lesser extent. Cursory examination of observations of fronts show this to be a realistic aspect of these moist simulations. This stronger warm flow and the narrow region of ascent ahead of the frontal surface have a clear interpretation in terms of the "warm conveyor belt" described by Browning and Monk (1982).

*d. Condensation heating*

The domain-averaged value of $\theta - \theta_0$ indicates the net heating due to condensation. The following average was computed in physical space:

$$\overline{\theta'}^{x,y} = \frac{1}{2Lh} \int_0^{2L} \int_0^h [\theta - \theta(t=0)]\, dx dz.$$

For $k = 0.80$ the moist mode has values of $\overline{\theta'}^{x,y}$ at $t$ = (0, 0.5, 1.0, 1.5, 2) days of $\overline{\theta'}^{x,y}$ = (0, 0, 0.15, 0.40, 0.79) $K$.

*e. Vertical velocity structure*

In Fig. 7 there is a double vertical velocity maximum apparent at $t = 1.5$ days which coalesces into a single maximum by $t = 2$ days. This is likely to be due to the difference in tilt of the region of ascent of the moist normal mode compared to the initial dry normal mode. As part of the adjustment, the large slope of the moist ascent becomes locally established at lower levels compared to the smaller slope of the ascent aloft. It is intriguing to speculate whether such a structure occurs in nature as moist processes become dominant in the baroclinic wave development. Orlanski and Ross (1984) have discussed a double maximum which occurs in their mesoscale simulation of a cold front. The simulation for $k = 1.27$ did not exhibit this feature.

As is the case in the two-layer model, there is an extremely large horizontal gradient of vertical velocity on the cold side of the ascent region. This also occurs in the dry solutions (see Fig. 6) but is particularly noticeable in the moist case. Given that cloud and rain are proportional to the vertical velocity we may expect that the thickest cloud and most intense precipitation are likely to be adjacent to the cloud-free cold air. This is in accord with observations of rapid clearing behind cold fronts.

*f. Surface pressure field*

In the presence of moist processes, the exponential rate of deepening of the surface pressure minimum is much accelerated. For example, in the case of $k = 0.80$ the following shows the difference between the surface maximum and minimum pressure deviation ($\Delta p$) as a function of time: for $t$ = (0, 0.5, 1, 1.5, 2) days, $\Delta p$ = (8, 11.5, 17.5, 27.0, 43.4) mb. The final 12 hours before frontal collapse shows a pressure fall of about 16 mb, which exceeds the threshold for explosive development defined by Sanders and Gyakum (1980). It is likely, however, that the inclusion of modest amounts of surface dissipation would substantially reduce this deepening rate. It seems unlikely that condensation effects on normal-mode growth can by themselves explain extreme cases of cyclogenesis such as those reported by Sanders and Gyakum (1980), especially as condensation is not peculiar to oceanic storms.

Although not shown here, the shape of the surface pressure field, analogous to the trace on a barograph, is similar to that shown for the two-layer model in Fig. 5b. This is a characteristically different shape from that of the dry wave, where the trace remains nearly sinusoidal right up to frontal collapse, with a change in curvature across the front. In the moist case the trace essentially keeps the same sign curvature (in space or time) across the front. This seems to be typical of barograph traces of rapidly deepening lows.

*g. Evolution of potential vorticity*

The form of the potential vorticity equation (29) shows that latent heat release will produce a lower troposphere positive anomaly and an upper troposphere negative anomaly of potential vorticity. This is subject to the mass-weighted volume integral remaining constant. The moist simulations indeed show this to be the case (e.g., see Fig. 8). However, unlike the results described by Thorpe and Emanuel (1985) for deformation-forced frontogenesis, these anomalies are advected horizontally through the baroclinic wave by the total wind field, which contains the background zonal shear flow. Moving with the cyclone, this produces an advection of the anomaly in the direction of the cold air at low levels and in the direction of the warm air at upper levels (or in the figures, from right to left at low levels and vice versa aloft). In terms of potential vorticity, this spreads the influence of the condensation from the ascent region into the descent region. This does not diminish the growth of the baroclinic wave but it does have important implications for its structure.

The potential vorticity concepts developed by Hoskins et al. (1985) can be used here to describe these implications. In that paper it was shown that a positive potential vorticity anomaly is consistent with a balanced flow which has cyclonic relative vorticity and an increased static stability; the opposite signs apply for a negative anomaly. The proportion of the stability and circulation anomalies depends on the aspect ratio of the potential vorticity anomaly but is typically shared equally. These ideas allow us to predict that in moist baroclinic waves there is an increase in stability and cyclonic vorticity at low levels and a decrease at upper levels due to the condensation. Because of horizontal advection, this occurs not only where the condensation is located but, in time, throughout the wave. As an example, for $k = 0.94$ in the dry simulation after 3 days the absolute vorticity maximum and minimum are the same at the upper and lower boundary with values of $2.9f$ and $0.6f$. In the moist simulation at 1.5 days at the lower boundary they are $3.65f$ and $0.7f$, while at the upper boundary they are $1.4f$ and $0.57f$. The increase in stability at low levels and decrease at upper levels is particularly evident in Fig. 7a for $k = 0.80$.

*h. Neutral mode growth*

When $k = 1.27$ the dry initial perturbation is a neutral normal mode, as its horizontal scale is shorter than the short wave cutoff. Without moist processes this does not grow but propagates at 2.5 m $s^{-1}$ in the model frame of reference. [It is worth noting here that the growing moist modes do not propagate, in agreement with the analytic result (appendix B) that $\sigma$ cannot be complex. The location of the frontal collapse is, however, slightly different in the moist case, being displaced some 300 km eastward relative to the dry simulation.] In the presence of condensation, the wave initially propagates but quickly becomes stationary as the wave develops. The moist mode grows rapidly despite being initiated with a perturbation which does not have the correct phase tilts for baroclinic development. This shows that an important role of moist processes in the atmosphere is to allow baroclinic development on horizontal scales otherwise stable to baroclinic instability.

## 6. Conclusions

We have examined the structure and growth rate of baroclinic waves developing in environments characterized by small or zero moist potential vorticity, a condition often observed in middle latitudes. Analytic solutions of a two-layer semigeostrophic model show that the growth rate at zero moist potential vorticity is about 2.5 times the classical dry value and that the updraft collapses onto a thin ascending sheet. The wavelength of the most unstable moist mode when $q_{ge} = 0$ is roughly 60% of the dry value. In the moist model atmosphere frontal collapse occurs first at the surface despite the presence of a rigid upper boundary. These results are confirmed by numerical integrations of a multilevel semigeostrophic model which show, in addition, that the total wind, which contains the base state zonal shear, advects through the horizontal extent of the wave high potential vorticity generated at low levels and low potential vorticity produced at upper levels by condensation. The distributions of wind, temperature, and pressure in the moist models appear closer to observed distributions than those of dry models. While condensation effects increase the growth rate of baroclinic normal modes, the authors do not believe that this alone can account for cases of explosive marine cyclogenesis. This conclusion is consistent with those of previous investigators (e.g., Anthes et al., 1983).

We emphasize that we have not examined the effects of unstable moist stratification (i.e., $q_{ge} < 0$) on developing baroclinic waves; rather, we have investigated the characteristics of disturbances growing in an environment which is nearly neutral to slantwise moist convection. Such effects, together with those of surface friction, surface heat fluxes, and three-dimensionality remain to be explored in future work.

*Acknowledgments.* Drs. Thorpe and Emanuel would like to acknowledge receipt of a NATO Grant 129/84 which enabled the necessary collaboration to take place. Authors Emanuel and Fantini were supported in part by National Science Foundation Grant ATM-8513871.

## APPENDIX A

### General Solution of the Eigenvalue Problem

In each of the regions 1 and 2, the antisymmetric parts of the solutions to (43) may be written

$$\psi_{1,2} = A_{1,2} \sinh(\alpha_{1,2} X) + B_{1,2} \sinh(\beta_{1,2} X), \quad \text{(A1)}$$

where $X$ is defined separately in each region (see Fig. 1) and $\alpha$ and $\beta$ (which may be complex) satisfy

$$(\alpha_{1,2}^2, \beta_{1,2}^2) = \frac{1}{2}\left\{\sigma^2 - \frac{2}{q} \pm \left[\left(\sigma^2 - \frac{2}{q}\right)^2 - \frac{8\sigma^2}{q}\right]^{1/2}\right\}, \quad \text{(A2)}$$

where the positive root yields $\alpha$ and the negative root gives $\beta$. $q$ is defined separately in each region according to (40). According to the boundary conditions and the subsequent discussion in the text, we require that $\partial\psi/\partial X$ vanish at the boundaries of the regions and that $\psi$, $q\partial^2\psi/\partial X^2$ and $q\partial^3\psi/\partial X^3$ be continuous across the internal boundaries. The vanishing of $\partial\psi/\partial X$ at the boundaries leads to the conditions

$$\left.\begin{aligned} A_1\alpha_1 \cosh\alpha_1 L_1 + B_1\beta_1 \cosh\beta_1 L_1 = 0 \\ A_2\alpha_2 \cosh\alpha_2 L_2 + B_2\beta_2 \cosh\beta_2 L_2 = 0 \end{aligned}\right\}. \quad \text{(A3)}$$

We use (A3) to eliminate $A_1$ and $A_2$ in favor of $B_1$ and $B_2$.

The other three conditions overspecify the eigenvalue problem and thus lead to the requirement that the determinants of two separate matrices vanish. These may be written

$$\begin{bmatrix} r\beta_1(\beta_1^2 - \alpha_1^2) & -\beta_2(\beta_2^2 - \alpha_2^2) \\ \tanh\beta_1 L_1 - \dfrac{\beta_1}{\alpha_1}\tanh\alpha_1 L_1 & \tanh\beta_2 L_2 - \dfrac{\beta_2}{\alpha_2}\tanh\alpha_2 L_2 \end{bmatrix} \begin{bmatrix} B_1 \cosh\beta_1 L_1 \\ B_2 \cosh\beta_2 L_2 \end{bmatrix} = 0, \quad \text{(A4)}$$

$$\begin{bmatrix} r\beta_1(\beta_1^2 - \alpha_1^2) & -\beta_2(\beta_2^2 - \alpha_2^2) \\ r[\beta_1^2 \tanh\beta_1 L_1 - \alpha_1\beta_1 \tanh\alpha_1 L_1] & \beta_2^2 \tanh\beta_2 L_2 - \alpha_2\beta_2 \tanh\alpha_2 L_2 \end{bmatrix} \begin{bmatrix} B_1 \cosh\beta_1 L_1 \\ B_2 \cos\beta_2 L_2 \end{bmatrix} = 0. \quad \text{(A5)}$$

With $r$ and $L_2$ specified, these may both be considered to yield eigenvalues $\sigma$ as functions of $L_1$. Except in certain cases, these two functions intersect only at a discrete set of points which yield the eigenvalues $\sigma$ and $L_1$. This set turns out to be countably infinite, but for all eigenvalues except one, the sign of the vertical velocity changes within either or both regions, making those solutions unacceptable. The acceptable eigenvalue $(\sigma, L_1)$ is found numerically for different values of $r$ and $L_2$ by searching for solutions of (A4) and (A5).

## APPENDIX B

### Proof That $\sigma$ is Not Complex

The proof that $\sigma^2$ is real is carried out as follows. Multiply (42) by $\psi^*$, the complex conjugate of $\psi$, and integrate over an entire wavelength $L$. For simplicity, we avoid having the endpoints of the integration at points where $w$ changes sign. We have

$$\underbrace{\int_0^L \psi^* \frac{\partial^3}{\partial X^3} q \frac{\partial\psi}{\partial X} dX}_{[1]} - \sigma^2 \underbrace{\int_0^L \psi^* \frac{\partial}{\partial X} q \frac{\partial\psi}{\partial X} dX}_{[2]} + 2\underbrace{\int_0^L \psi^* \frac{\partial^2\psi}{\partial X^2} dX}_{[3]} + 2\sigma^2 \int_0^L |\psi|^2 dx = 0. \quad \text{(B1)}$$

Integrating terms 1, 2 and 3 in (B1) by parts and noting that $\psi$ is periodic over $L$, each of these terms may be written

$$\left.\begin{aligned} &[1] \int_0^L \frac{\partial^2\psi^*}{\partial X^2}\frac{\partial q}{\partial X}\frac{\partial\psi}{\partial X} dX + \int_0^L q\left|\frac{\partial^2\psi}{\partial X^2}\right| dX \\ &\qquad [a] \\ &[2]\ \sigma^2 \int_0^L q\left|\frac{\partial\psi}{\partial X}\right|^2 dX \\ &[3]\ -2\int_0^L \left|\frac{\partial\psi}{\partial X}\right|^2 dX \end{aligned}\right\}. \quad \text{(B2)}$$

Since $q$ has finite jumps at points where $w$ changes sign, the term labeled [a] above has delta functions in the integrand. But because $\partial\psi/\partial X$ is by definition zero at these points, term [a] vanishes. Using this fact and the other relations (B2), (B1) may be written

$$\int_0^L q\left|\frac{\partial^2\psi}{\partial X^2}\right|^2 dX + \sigma^2 \int_0^L q\left|\frac{\partial\psi}{\partial X}\right|^2 dX - 2\int_0^L \left|\frac{\partial\psi}{\partial X}\right|^2 dX + 2\sigma^2 \int_0^L |\psi|^2 dX = 0. \quad \text{(B3)}$$

The imaginary part of the above is

$$2\sigma_r\sigma_i \int_0^L \left[q\left|\frac{\partial\psi}{\partial x}\right|^2 + 2|\psi|^2\right] dX = 0. \quad \text{(B4)}$$

Since the integrand of (B4) is positive definite, $\sigma_i$ must vanish everywhere except when $\sigma_r = 0$.

## APPENDIX C

### Asymptotic Solutions for Small $r$

Asymptotic solutions to the equations (43) with boundary conditions can be found by expanding the eigenvalues in powers of $r$. The process of finding these solutions is simplified by noting certain behavior in the numerical solutions. Specifically, we suppose that the coefficients $A_1$ and $B_2$ defined by (A1) are order one quantities and that $L_1 \approx O(r^{1/2})$ in the limit of small $r$. We also note from the definitions of $\alpha_1, \beta_1$ (see A2) that to O(1)

$$\left.\begin{aligned}\alpha_1^2 &= -\sigma^2 + O(r^{1/2}) \\ \beta_1^2 &= -2/r + 2\sigma^2 + O(r^{1/2})\end{aligned}\right\}. \tag{C1}$$

Following the same procedure outlined in appendix A but formulating the matrices for the coefficients $A_1$ and $B_2$ (rather than $B_1$ and $B_2$) results in the following two simultaneous equations valid to O($r$):

$$\beta_1[\alpha_2 \tanh\alpha_2 L_2 - \beta_2 \tanh\beta_2 L_2] = (\beta_2^2 - \alpha_2^2)\tanh\beta_1 L_1, \tag{C2}$$

$$r(\beta_1^2)\left[\frac{\beta_2}{\alpha_2}\tanh\alpha_2 L_2 - \tanh\beta_2 L_2\right] = \beta_2(\beta_2^2 - \alpha_2^2)\left(\frac{1}{\beta_1}\tanh\beta_1 L_1 - L_1\right), \tag{C3}$$

where the hyperbolic tangents of $O(r^{1/2})$ quantities have been expanded to $O(r^{1/2})$. If $\tanh\beta_1 L_1$ is O(1), the above implies that $\beta_2 \to \alpha_2 + O(r^n)$, where $n$ is some positive number, since $\beta_1^{-1}$ and $L_1$ vary as $r^{1/2}$. But this is inconsistent since no matter how $\alpha_2$ and $\beta_2$ approach each other the terms in brackets on the left-hand side of (C2) and (C3) have the same order of $r$ as the term $(\beta_2^2 - \alpha_2^2)$. Thus the only consistent solutions are for $\tanh\beta_1 L_1 = O(\beta_1) = O(r^{-1/2})$. Elimination of $\tanh\beta_1 L_1$ from (C2) and (C3) then yields the dispersion relation

$$\frac{2+\alpha_2^2}{\alpha_2}\tanh\alpha_2 L_2 = \frac{2+\beta_2^2}{\beta_2}\tanh\beta_2 L_2, \tag{C4}$$

correct to O(1). Since $\alpha_2$ and $\beta_2$ depend only on $\sigma$ (and not on $r$) the above yields the dispersion relation $\sigma(L_2)$ valid in the limit of $r \to 0$. This is solved numerically with the results plotted in Fig. 2. The growth rate reaches a peak value of 1.484 when $L_2 = 1.94$, and quickly asymptotes to $\sqrt{2}$ at large $L$. We can solve (C2) for the quantity $\beta_1^{-1}\tanh\beta_1 L_1$; at the value of $L_2$ at which the growth rate peaks, this has the value −0.477. Since $\beta_1 = i\sqrt{2/r}$ as $r \to 0$, this yields

$$\tan\sqrt{2/r}L_1 = -0.477\sqrt{2/r} \quad \text{as} \quad r \to 0.$$

If we let $\sqrt{2/r}L_1 \to (\pi/2) + \epsilon$, where $\epsilon$ is a small parameter, expansion of the above gives

$$\epsilon \approx \sqrt{2r}.$$

Thus in the limit of small $r$,

$$\lim_{r\to 0} L_1 = \frac{\pi}{2\sqrt{2}}\sqrt{r} + r. \tag{C5}$$

This function is plotted alongside the numerical results in Fig. 3.

## REFERENCES


Anthes, R. A., Y.-H. Kuo and J. R. Gyakum, 1983: Numerical simulations of a case of explosive marine cyclogenesis. *Mon. Wea. Rev.*, **111**, 1174–1188.

Bennetts, D. A., and B. J. Hoskins, 1979: Conditional symmetric instability—a possible explanation for frontal rainbands. *Quart. J. Roy. Meteor. Soc.*, **105**, 945–962.

Bjerknes, J., 1919: On the structure of moving cyclones. *Geofys. Pub.*, Norske Videnskaps-Akad., 1–8.

Browning, K. A., and G. A. Monk, 1982: A simple model for the synoptic analysis of cold fronts. *Quart. J. Roy. Meteor. Soc.*, **108**, 435–452.

Cullen, M. J. P., and R. J. Purser, 1984: An extended Lagrangian theory of semigeostrophic frontogenesis. *J. Atmos. Sci.*, **41**, 1477–1497.

Emanuel, K. A., 1985: Frontal circulations in the presence of small moist symmetric stability. *J. Atmos. Sci.*, **42**, 1062–1071.

——, 1986: An air–sea interaction theory for tropical cyclones. Part I: Steady state maintenance. *J. Atmos. Sci.*, **43**, 585–604.

Heckley, W. H., 1980: Frontogenesis. Ph.D. Thesis, University of Reading.

Hoskins, B. J., 1975: The geostrophic momentum approximation and the semigeostrophic equations. *J. Atmos. Sci.*, **32**, 233–242.

——, 1976: Baroclinic waves and frontogenesis. Part I: Introduction and Eady Waves. *Quart. J. Roy. Meteor. Soc.*, **102**, 103–122.

——, and F. P. Bretherton, 1972: Atmospheric frontogenesis models: Mathematical formulation and solution. *J. Atmos. Sci.*, **29**, 11–37.

——, M. E. McIntyre and A. W. Robertson, 1985: On the use and significance of isentropic potential vorticity maps. *Quart. J. Roy. Meteor. Soc.*, **111**, 877–916.

Orlanski, I., and B. B. Ross, 1984: The evolution of an observed cold front. Part II: Mesoscale dynamics. *J. Atmos. Sci.*, **41**, 1669–1703.

Phillips, N. A., 1951: A simple three-dimensional model for the study of large-scale extratropical flow patterns. *J. Meteor.*, **8**, 381–394.

Sanders, F., and J. R. Gyakum, 1980: Synoptic-dynamic climatology of the "bomb". *Mon. Wea. Rev.*, **108**, 1589–1606.

Thorpe, A. J., and K. A. Emanuel, 1985: Frontogenesis in the presence of small stability to slantwise convection. *J. Atmos. Sci.*, **42**, 1809–1824.